ARTICLE   OPEN

Check for updates

Segregation-assisted spinodal and transient spinodal phase separation at grain boundaries

Reza Darvishi Kamachali [1,2 ✉], Alisson Kwiatkowski da Silva [2], Eunan McEniry[2], Dirk Ponge[2], Baptiste Gault [2,3], Jörg Neugebauer[2] and Dierk Raabe[2]

Segregation to grain boundaries affects their cohesion, corrosion, and embrittlement and plays a critical role in heterogeneous nucleation. In order to quantitatively study segregation and low-dimensional phase separation at grain boundaries, here, we apply a density-based phase-field model. The current model describes the grain-boundary thermodynamic properties based on available bulk thermodynamic data, while the grain-boundary-density profile is obtained using atomistic simulations. To benchmark the performance of the model, Mn grain-boundary segregation in the Fe–Mn system is studied. 3D simulation results are compared against atom probe tomography measurements conducted for three alloy compositions. We show that a continuous increase in the alloy composition results in a discontinuous jump in the segregation isotherm. The jump corresponds to a spinodal phase separation at grain boundary. For alloy compositions above the jump, we reveal an interfacial transient spinodal phase separation. The transient spinodal phenomenon opens opportunities for knowledge-based microstructure design through the chemical manipulation of grain boundaries. The proposed density-based model provides a powerful tool to study thermodynamics and kinetics of segregation and phase changes at grain boundaries.

INTRODUCTION

Grain boundaries (GBs) influence functional and structural properties of polycrystalline materials in different ways. They can have both positive (strengthening in terms of the Hall–Petch effect) and negative (weakening due to corrosion or formation of precipitation-free zones) influence on the material's performance. Hence, studying and engineering GBs are crucial for optimizing microstructure and material properties[1,2]. The vast structural variability and high amenability of GBs to chemical changes renders them ideal objects for tuning their properties by solute segregation[3–7]. From a thermodynamic point of view, a GB has distinct phase-like behavior[8] and may undergo confined structural and chemical transitions as evidenced in several systems[9–11]. Compared to bulk materials, a GB is subjected to additional (geometric) constraints that result in structural and compositional gradients within the GB region. GB phases are hence sometimes referred to as complexions[11–13] to distinguish them from bulk phases.

In alloys, the properties of GBs are expected to closely correlate with their composition. This becomes particularly important when solute atoms segregate to the GBs. The segregation is thermodynamically driven by a reduction in the total energy of the system. Segregation not only alters the local kinetics[14–19] and mechanical properties of a GB[20–23], but also influences thermodynamic driving forces for heterogeneous nucleation such as in GB precipitation[24–28], phase transformations[29–31], and premelting[32,33]. Segregation can also result in low-dimensional phase separation forming solute-poor and solute-rich regions inside the GB plane. This has been indeed postulated by Fowler and Guggenheim[34] and Hart[35,36] that an interface/GB region exhibiting similar properties to a regular condensed solution might undergo such a phase separation. The resulting low-dimensional spinodal phase separation into high and low segregation regions can

produce precursor states for the formation of new phases[37,38]. The new phases then can be either confined to the GB region, as in GB precipitation, or expand as a regular volume phase into the adjacent bulk.

In reality, one expects segregation, phase separation, and nucleation of a new phase to occur hand in hand. In order to describe such convoluted process, the thermodynamics and kinetics of GB segregation must be studied quantitatively. Extensive efforts have been made to apply surface adsorption models[8,34,39,40] for understanding GB segregation[35,41–45]. Assessing GB thermodynamic and kinetic properties, however, remains a challenging task due to the complex nature of GBs[1]. To address this problem, several models have been developed. For example, to account for changes in thermodynamic properties of GB, variations in the local coordination number (broken bond model) of the defected GB structure were considered (for details see refs. [46–48] and references therein). In a recent study, we have employed this model to investigate GB segregation in magnetic Fe–Mn system[38].

In parallel to the conventional thermodynamic models, phase-field models have been developed to study GB-related phenomena which concentrate on the effect of non-local gradient energy terms within the GB region. The seminal work of Cahn[49] highlighted the importance of the concentration gradient energy term in the vicinity of an interface and its effect on the critical wetting transition. Since then several phase-field studies were conducted on the thermodynamic and kinetic effects of solute segregation (see, for instance, refs. [50–54]). Hu and Chen[55] developed a phase-field model for studying solute segregation and phase transition at dislocations. Ma et al. combined Cahn's non-local concentration gradient model with the idea of variation in local coordination number to describe phase transition and solute drag at GBs and dislocations[56,57]. Mishin has further

R. Darvishi Kamachali et al.

extended this model in a recent study[58]. Based on the Kobayashi, Warren, and Carter (KWC) model for GBs[59], Tang et al. developed a phase-field model that describes order–disorder transitions in pure systems[60,61] and phase transition in binary alloys[62]. Kim et al.[63] reviewed thermodynamic aspects of some phase-field models for GB segregation and proposed a phase-field model for GB segregation which uses the equal diffusion potential condition[64], i.e., defining two concentration fields for the bulk and GB, separately, however, neglecting consideration of the concentration gradients across the GB region.

In the current study, we use a density-based phase-field model to study interfacial segregation and phase separation. In this picture, the structurally defected GB region is represented by a continuous atomic density field, varying across the GB region, with reference to the adjacent homogeneous bulk. The density-based model then allows us to approximate GB free energy functional based on available bulk thermodynamic data. Detailed derivation of the density-based theory can be found in ref. [65]. Using atomistic simulations, the atomic density profile across the GB region is determined. We study here the Fe–Mn system in which the segregation of Mn in BCC Fe plays a critical role in GB embrittlement and formation of austenite. ThermoCalc databases were used to obtain thermodynamic and kinetic information for the Fe–Mn system. In the "Results" section, the details of our model and the results of our simulation and experimental studies are presented. Segregation isotherms and spatial segregation patterns within a GB were studied. While the equilibrium segregation isotherms indicate only a single critical bulk composition related to the GB spinodal (discontinuous jump in the GB segregation), our study reveals that a transient GB spinodal phase separation, lasting for a finite period of time, can occur for a range of alloy compositions. Using the concept of transient spinodal, a consistent explanation of GB segregation behavior in three Fe–Mn alloys, namely Fe–3.0 at.% Mn, Fe–4.0 at.% Mn, and Fe–8.6 at.% Mn, is obtained. The existence and significance of a segregation-assisted transient spinodal phenomenon and its potential application for designing desirable microstructures are presented in the "Discussion" section.

RESULTS

Density-based phase-field model

In a GB, atoms are forced to accommodate for the incompatible lattices of the two adjacent grains. This results in a different atomic density in the GB region, when compared to the corresponding bulk values. In his seminal work, van der Waals[66] showed that the energy of an interface can be described as a function of mass density and its variations (gradients) within the interface region. In contrast to Gibbs's model[8] which assumes a mathematically sharp interface, in this picture an interface is a heterogeneous domain across which the density profile varies continuously albeit very sharply. For a GB, one expects a similar density variation confined to the GB region. The Gibbs free energy density of a GB in a pure substance made of atomic species A can be obtained as

$$G^{\mathrm{GB}}(T,\rho) = E_A^{\mathrm{B}}(\rho^2 - 1) + C_A^{\mathrm{B}}(\rho - 1) + \frac{\kappa_\rho}{2}(\nabla\rho)^2 . \tag{1}$$

Here the superscripts B and GB represent the bulk and GB properties, respectively. κ_ρ is the density gradient coefficient, E_A^{B} is the potential energy, which is a function of the atomic arrangement in the system, and $C_A^{\mathrm{B}} = K_A^{\mathrm{B}} + pV_A^{\mathrm{B}} - TS_A^{\mathrm{B}}$ is the sum of kinetic (K_A^{B}), mechanical energy (pV_A^{B}) and entropic ($-TS_A^{\mathrm{B}}$) energy contributions of the bulk material at a given temperature T and pressure p. For solid-state materials, the kinetic energy is negligible but the mechanical energy can be significant and also density-dependent. In the present study, however, as a first attempt we simplify our model neglecting both of these

terms:

$$C_A^{\mathrm{B}} \approx -TS_A^{\mathrm{B}} . \tag{2}$$

In Eq. (1), we use a dimensionless atomic density field $\rho(\vec{r},t)$ which defines the number of atoms per unit volume, i.e., the spacing between the atoms, at any given point. The atomic density field varies across the system continuously, such that $\rho = \rho^B = 1$ inside the bulk (far from the GB) and $\rho < 1$ inside the GB region. In the center of the GB, $\rho = \rho^{\mathrm{GB}} < 1$ marks the minimum GB atomic density at the GB plane. In principle, the atomic density within a GB plane fluctuates. This is, however, neglected in the current treatment, assuming an average constant GB density value ρ^{GB} corresponding to the GB type. The relative atomic density field ρ can be related to the atomistic description of the system by choosing a coarse-graining length comparable to the cut-off radius in the atomistic simulations, further discussed in the Supplementary Discussion. Hence the GB density value ρ^{GB} can be obtained using atomistic simulations.

The atomic density field and its spatial gradients account for the structural inhomogeneities in the system, i.e., across the GB. Here the potential energy and entropy terms in Eq. (1) turn out to scale differently with the atomic density ρ. The C_A^{B} term scales linearly with the atomic density that is proportional to the number of atoms per unit volume, which differs between the bulk and GB. The potential energy, however, scales quadratically with the density. In this case, the extra density coefficient is proportional to the bonding energies (force density) in the elastic limit that changes with interatomic distance. Finally, the gradient term in Eq. (1) is a correction to the potential energy due to the spatial density change within the GB region. Equation (1) allows an approximation of the GB free energy based on the bulk thermodynamic data. A thorough description of the density-based theory is given in ref. [65].

For a binary system, the mixing enthalpy and entropy terms have to be considered. For the sake of simplicity, we neglect the scaling of the mixing entropy $\Delta S_{\mathrm{mix}}(T, X_B)$ with the atomic density. The enthalpy of mixing $\Delta H_{\mathrm{ex}}(T, \rho, X_B)$, however, may be strongly influenced by the chemical and structural environment. Motivated by the first term in Eq. (1), one can write

$$\Delta H_{\mathrm{ex}}(T, \rho, X_B) = \rho^2 \Delta H_{\mathrm{ex}}^{\mathrm{B}}(T, X_B) \tag{3}$$

in which $\Delta H_{\mathrm{ex}}^{\mathrm{B}}(T, X_B)$ is the excess enthalpy of the bulk solution. For the Fe–Mn system, this will be the sum of chemical and magnetic mixing enthalpies. Using Eqs. (1)–(3), the total Gibbs free energy density of a heterogeneous dilute binary system (containing a GB) can be written as

$$\begin{aligned} G_{\mathrm{alloy}}(T,\rho,X_B) &= G^{\mathrm{B}}(T,X_B,\rho=1) + G^{\mathrm{GB}}(T,\rho) \\ &= X_A G_A^0(T) + X_B G_B^0(T) + \rho^2 \Delta H_{\mathrm{ex}}^{\mathrm{B}}(T,X_B) - T\Delta S_{\mathrm{mix}}^{\mathrm{B}}(T,X_B) \\ &\quad + \frac{\kappa_X}{2}(\nabla X_B)^2 + E_A^{\mathrm{B}}(\rho^2-1) - TS_A^{\mathrm{B}}(\rho-1) + \frac{\kappa_\rho}{2}(\nabla\rho)^2 \end{aligned} \tag{4}$$

where the subscripts B and A indicate solute (Mn) and solvent (Fe), respectively, with $X_A + X_B = 1$, G_i^0 is the Gibbs free energy of the pure bulk i and κ_X is the concentration gradient coefficient. In this work, the thermodynamic properties $G_A^0(T)$, $G_B^0(T)$, $\Delta H_{\mathrm{ex}}^{\mathrm{B}}(T,X_B)$, $\Delta S_{\mathrm{mix}}^{\mathrm{B}}(T,X_B)$, and S_A^{B} are numerically extracted from a commercial ThermoCalc database. Here the chemical inhomogeneity across the system is described by the concentration gradients while the atomic density gradients account for structural inhomogeneity across the GB region. The gradient coefficients κ_ρ and κ_X are obtained by combining atomistic simulations and bulk thermodynamic data, as discussed in the next section. For any point in the GB with atomic density $\rho < 1$, Eq. (4) gives an approximation of the GB Gibbs free energy density. Inside the homogeneous bulk phase, $\rho = 1$, $\nabla\rho = 0$, $\nabla X_B = 0$ and the Gibbs free energy of the bulk can be recovered:

$$G_{\mathrm{alloy}}^{\mathrm{B}} = X_A G_A^0(T) + X_B G_B^0(T) + \Delta H_{\mathrm{ex}}^{\mathrm{B}}(T,X_B) - T\Delta S_{\mathrm{mix}}^{\mathrm{B}}(X_B). \tag{5}$$

The current density-based phase-field model can be also understood as a generalization of the previous model by Ma et al.[56], where the atomic density field can be imagined as a coarse-grained coordination number on the continuum mesoscale level. Using the continuum atomic density parameter here the coarse-grained coordination number can be seen as equivalent to the average interatomic distances among the atoms as well. The atomic density parameter enables a 'mean-field' approximation of the GB environment with reference to the adjacent bulk phase[65]. Compared to the classical phase-field models, since the atomic density field can be defined based on atomistic simulations, it can provide more quantitative physical interpretation of this field variable. The density and concentration fields have two separate gradient energy contributions that account for the structural and compositional inhomogeneities across the system, respectively. Together, the coupled evolution of the density and concentration fields regulates the magnitude and spread of the segregation profile across the GB region and determines the tendency for an interfacial spinodal decomposition.

In this work, we study GB segregation in polycrystalline Fe–Mn alloys with large grain size. The polycrystalline alloy samples with free surfaces are isothermally heat-treated at 450 °C under 1 atm. pressure. We simulate a single flat GB section, as a subset of the polycrystalline body, separating two large grains where 'large' refers to a sufficiently large-grain volume so that (i) the given GB section does not interact with other GBs in the polycrystalline and (ii) a sufficiently high supply of Mn is available so that the in-grain composition remains practically unchanged during the Mn segregation. Hence the bulk composition at the boundaries of the simulation domain is fixed (parallel to the GB plane) and the total amount of solute atoms within the simulated domain is not conserved. The Gibbs free energy is the appropriate thermodynamic potential to describe this open thermodynamic system at constant temperature and pressure[67–69]. The local solute concentration field obeys the continuity equation that minimizes the Gibbs free energy with respect to the concentration field as

$$\dot{X}_B = -\nabla \cdot \mathbf{J}_B = \nabla \cdot \left[M X_B \nabla \frac{\delta \mathcal{G}}{\delta X_B} \right]. \tag{6}$$

Here $\mathcal{G} = \int G_{\text{alloy}} \, dV$ is the Gibbs free energy functional, δ indicates functional derivatives and M is the concentration-dependent atomic mobility. Due to the segregation, the ratio of the Fe and Mn atoms and therefore the equilibrium interatomic distances within the GB region change, such that the total Gibbs free energy is minimized with respect to the atomic density field. When the atoms relax to their new equilibrium positions, the total number of atoms in the simulation domain can change as well, i.e., $\int \rho \, dV \neq$ Const., while the constant pressure across the system is maintained. In the absence of plastic deformation, the atomic density field varies by rapid relaxation of the interatomic bonds in the elastic regime. Hence, instead of a diffusion equation, the evolution of the atomic density field is described by the relaxation equation

$$\dot{\rho} = -L \frac{\delta \mathcal{G}}{\delta \rho}. \tag{7}$$

Here L is a positive mobility factor. As a diffusion-controlled process, the kinetics of segregation is governed by the mobility of Mn solute atoms while the atomic density field evolves much faster by elastic bond relaxation. To assure the diffusion-controlled kinetics, a large value for L is chosen compared to the atomic mobility M. The atomic mobility of Mn in the Fe–Mn system is extracted from ThermoCalc MOB04 database. The thermodynamic properties required for Eq. (4) are extracted from commercial ThermoCalc TCFE9 database. In order to obtain realistic values for the GB density and energy ρ^{GB} and γ_A, atomistic simulations have been performed for a $\Sigma9\{122\}[1\bar{1}0]$ symmetric tilt GB in pure α-Fe,

using the environmental tight-binding approach described in refs. [70,71]. Further details and parameters are described in the "Methods" section.

Assessment of the model parameters

Since the current model and methodology can be applied for studying GB segregation and related phenomena in different materials, the associated model parameters are discussed. A further developed version of the density-based model is presented elsewhere[65].

For a flat GB in a pure substance, the equilibrium atomic density profile across the GB follows:

$$\rho_{\text{eq}}(x) = \begin{cases} \left(\frac{1+\rho^{\text{GB}}}{2} \right) - \left(\frac{1-\rho^{\text{GB}}}{2} \right) \cos\left(\frac{\pi x}{\eta} \right) & \text{if } -\eta \leq x \leq \eta \\ 1 & \text{else} \end{cases} \tag{8}$$

$$\text{with} \quad \eta = \pi \sqrt{\frac{\kappa_\rho}{-2E_A^B}} \tag{9}$$

which satisfies $2E_A^B \rho + C_A^B - \kappa_\rho \nabla^2 \rho = 0$ with $\rho(x=0) = \rho^{\text{GB}}$, $\rho(x = \pm\eta) = 1$, and $\nabla\rho(x=0) = 0$ that allows for a continuous atomic density profile across the GB. Compared to an order parameter as in classical phase-field models, the atomic density field is a spatially symmetric (two-sided) profile across the GB, as also confirmed by the atomistic simulations (Fig. 1). Such two-sided profile allows a spatial approximation of the free energy density (based on the bulk thermodynamic data) across the GB.

In Eqs. (8) and (9), 2η is the GB width. Experimentally, this width can be measured smaller because the atomic density is a smooth and continuous field across the GB. Choosing the coarse-graining radius based on the atomic cut-off radius[72], we can link the current mesoscale density-based phase-field model with the atomistic simulations. In this way, a more physical picture of the GB can be obtained. Inserting Eq. (8) in Eq. (1) gives the equilibrium GB energy $\gamma_A = a_0 \left(1 - \rho^{\text{GB}}\right)^2$ with $a_0 = \frac{\pi}{4} \sqrt{-2E_A^B \kappa_\rho}$. One can see that γ_A varies as a function of ρ^{GB}. When $\rho^{\text{GB}} \to 1$, the GB energy approaches zero. This situation can indeed be observed for the case of special, highly symmetric boundaries, such as for coherent twin boundaries with low coincidence values, where the GB energy is low and the local atomic density is close to that of the bulk.

The bulk potential energy E_A^B, the minimum atomic density ρ^{GB} at the GB, the gradient coefficient κ_ρ and the GB energy γ_A can be determined from atomistic simulations. In the current study, a symmetric tilt GB $\Sigma9\{122\}[1\bar{1}0]$ in α-Fe is simulated. The GB structure is fully relaxed using an environmental tight-binding approach, a methodology previously used to study light-element interactions with a broad set of GBs in α-Fe[70]. The current assessment can be generalized and applied for different types of GBs.

In order to obtain the continuous atomic density profile from atomistic simulations a Gaussian broadening scheme with various smearing radii β was applied. A physically sound choice of the coarse-graining length is to calculate the continuous atomic density over a spherical volume of the atomistic cut-off radius. This is motivated by the fact that all physical properties from atomistic simulations are calculated up to the cut-off radius[72]. Three different smearing radii close to the cut-off radius (~4 Å) were examined in our study.

By fitting the analytical solution given in Eq. (8) to the results from atomistic simulations, the corresponding values of the minimum GB atomic density ρ^{GB} and the GB width η can be obtained. The coarse-grained atomic densities and the fittings from Eq. (8) are shown in Fig. 1. With increasing the smearing radius in the atomistic simulations, the GB region becomes wider, the atomic density profile becomes smoother and the in-plane fluctuations of the GB density ρ^{GB} decrease. The coarse-grained
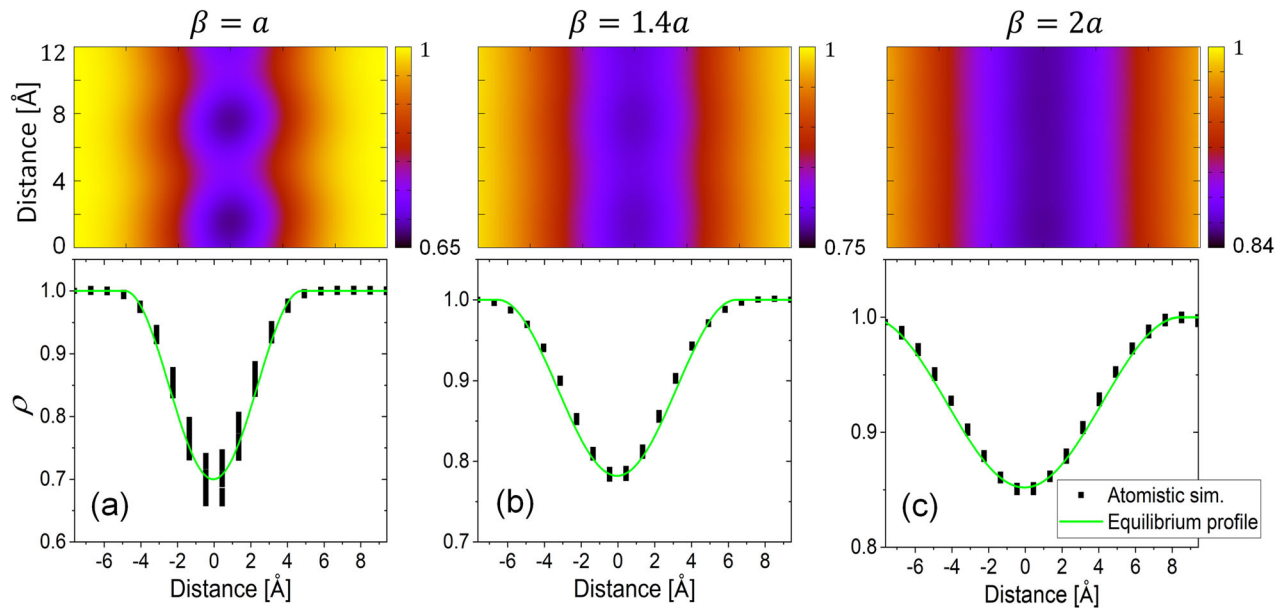
R. Darvishi Kamachali et al.

Fig. 1 Equilibrium density profile across a GB in α-Fe. The results of atomistic simulations are shown and fitted to the analytical solution shown in Eq. (8) (solid line). Three different smearing radii **a** $\beta = a$, **b** $\beta = 1.4a$ (atomistic cut-off radius), and **c** $\beta = 2a$, with the interatomic distance $a \sim 2.5$ Å, were examined to compare the results. Further discussion on the coarse-graining idea is provided in the "Methods" section.

atomic densities obtained from atomistic simulations are in good agreements with Eq. (8) and confirm the continuity of the coarse-grained atomic density field ρ across the GB.

In order to obtain the concentration gradient coefficient κ_X, the interface between the spinodally decomposed low- and high-concentration bulk phases must be studied. As proposed by Cahn and Hilliard[73], the energy of this interface between the two phases read

$$\gamma_I = \sqrt{2\kappa_X} \int_{X_{low}}^{X_{high}} \sqrt{\Delta G_{alloy}^B} \, dX. \tag{10}$$

Here ΔG_{alloy}^B is the excess grand potential of the two bulk phases in equilibrium. The Gibbs free energy and chemical potentials required to calculate ΔG_{alloy}^B are obtained from ThermoCalc thermodynamic database TCFE9. Equation (10) gives a direct relation between the gradient coefficient κ_X and the interface energy γ_I. Since the value for γ_I is not known for our system, we examine here κ_X values corresponding to $\gamma_I = 0.01$–0.1 J m^{-2}. In the following, we use the results from atom probe tomography (APT) measurements to adopt the best choice of γ_I (κ_X) and GB density ρ^{GB} in our studies.

Equilibrium segregation isotherms
In order to address interfacial phenomena in the Fe–Mn system, we first study the equilibrium segregation isotherms, i.e., the GB equilibrium concentration X_{Mn}^{GB} as a function of the bulk composition. We study Mn segregation in different Fe–Mn alloys annealed at 450 °C and conduct parametric studies to understand the effects of the GB atomic density ρ^{GB} and of the concentration gradient energy coefficient κ_X values on the segregation isotherms. The results are shown in Fig. 2. The values with closest agreement to the APT measurements were then taken for conducting 3D simulations.

The APT measurements revealed that at 450 °C a first order transition, marked by a distinct jump in the GB concentration, occurs for an alloy with a composition between 3.0 and 4.0 at.% Mn[38]. This composition range is marked in Fig. 2. The simulation results show that the segregation isotherm shifts to the left for a lower GB atomic density ρ^{GB}, i.e., the first order transition becomes possible for lower bulk compositions when the GB

density decreases. Importantly, Fig. 2 also shows that higher levels of GB segregation can be achieved for a lower gradient coefficient κ_X. The optimal values (with the least deviation from the APT results) for ρ^{GB} and κ_X are found to be 0.75 and 5×10^{-18} J m^2 mol^{-1}, respectively. These values are used for further investigations in the following.

Figure 3a shows the equilibrium GB concentration profiles obtained for different bulk compositions using $\rho^{GB} = 0.75$ and $\kappa_X = 5 \times 10^{-18}$ J m^2 mol^{-1}. The corresponding density profiles across the GB are shown in Fig. 3d and e. While the GB width slightly increases in terms of the density variations, we found an abrupt increase in Mn segregation level, from about 8 to 22 at.% Mn, when the bulk composition is changed by only 1 at.%, namely, from 3.0 to 4.0 at.% Mn. The equilibrium Mn segregations are confined to the GB region. From the experiments, three BCC Fe–Mn alloys with 3.0, 4.0, and 8.6 at.% Mn (in the following referred to as Fe3Mn, Fe4Mn, and Fe9Mn, respectively) were analyzed with respect to the Mn concentration (Fig. 3b and c).

In practice, segregation profiles across a GB can be asymmetric (Fig. 3b). This can be mainly due to the density difference of the adjoining atomic planes (with different atomic spacing) on the two sides of the GB. To account for this crystallographic feature, the current isotropic description of the atomic density field can be replaced with an anisotropic description. Broken bond models for GB segregation already suggest how to consider such asymmetry at the GB region[47,48]. A similar idea can be adopted to introduce an anisotropic atomic density field. A curvature in the GB influences the equilibrium bulk composition (Gibbs–Thomson effect) and thus may also result in asymmetric atomic density and segregation profiles. Nevertheless, the current simulation results based on the isotropic atomic density field and a flat GB show good agreements with the experiments, compared in Fig. 3a–c.

The simulation results show that for a constant concentration gradient coefficient κ_X, a higher segregation level results in a wider (but still confined) segregation region. A further detailed study over the bulk composition space suggests that the jump in Mn segregation occurs for an alloy with a composition close to Fe–3.33 at.% Mn in which the GB segregation level abruptly increases from ~11 to ~22.6 at.% Mn (see the "Methods" section).
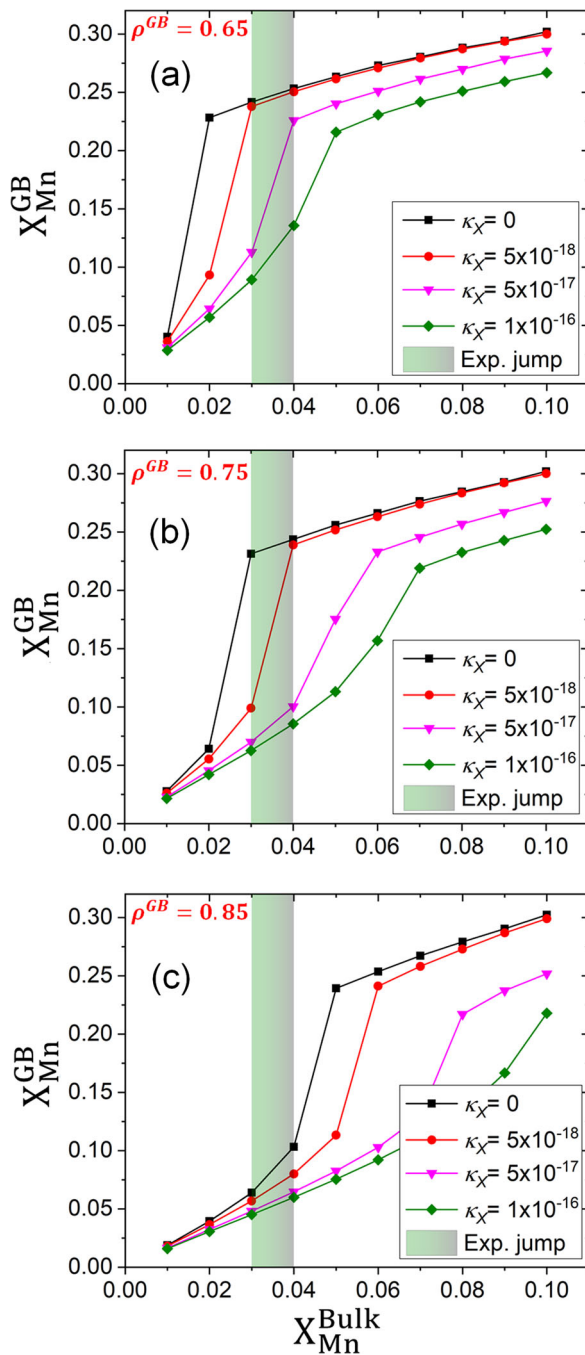
Fig. 2 GB segregation isotherms. Three different GB atomic densities were examined for (**a**) $\rho^{GB} = 0.65$, **b** $\rho^{GB} = 0.75$, and (**c**) $\rho^{GB} = 0.85$. The colored area indicates the composition range where the GB spinodal was observed experimentally. The jump in the segregation isotherms denotes the interfacial spinodal. A good match between the simulations and experiments is obtained for a GB atomic density of 0.75 and a gradient coefficient $\kappa_X = 5 \times 10^{-18}$ J m^2 mol^{-1}.

Interfacial transient spinodal

While 1D calculations provide direct insight into equilibrium segregation isotherms, 3D simulations are required to study kinetics and patterns of the segregation to GBs. 3D simulations of GB segregation were conducted for three Fe–Mn alloys with 2.9,

3.3, and 9.0 at.% Mn. The time evolution of the concentration field inside the GB plane is shown in Fig. 4. For an alloy with 2.9 at.% Mn (below the jump composition), the simulations show that the GB segregation starts immediately and increases monotonically. The equilibrium GB concentration of ~8 at.% Mn is achieved which remains unchanged even after 2.4×10^6 s (~28 days) at 450 °C. At the same time, the initial concentration fluctuations, in the range of up to ±1 at.%, decline and disappear. Similar results were obtained from the APT analysis for the Fe3Mn alloy annealed for 2 months at 450 °C (Fig. 5a and b): The GB is enriched with 8 at.% Mn, very close to the simulation results. The APT analysis shows that concentration fluctuations up to ±3 at.% exist inside the GB plane that remain stable even after the long-term annealing up to 2 months at 450 °C. These are associated with the atomic density fluctuations expected in a real GB. Nevertheless, the concentration fluctuations are about an order of magnitude below the experimentally observed chemical spinodal fluctuations as discussed in the following.

For an alloy with 3.3 at.% Mn (close to the jump), the simulations revealed an interfacial spinodal phase separation (Fig. 4). It was found that the initial GB segregation is followed by a gradual in-plane phase separation into low and high-concentration domains with ~8 and ~22 at.% Mn, respectively. Thereafter, islands with high-concentration level gradually grow and later coalesce to larger segregation islands. The segregation kinetics of these later stages, however, are very slow. For the Fe4Mn alloy annealed for 2 month at 450 °C, a jump in the segregation level was observed in the APT measurements (Fig. 5c and d) where the high and low concentration domains within the GB plane were observed next to each other.

The simulation results for a Fe–9 at.% Mn alloy show an even more interesting segregation behavior (Fig. 4). When the level of segregation at the GB increases up to the critical bulk composition for GB spinodal phase separation, our simulations reveal that the GB goes through a transient spinodal regime, i.e., an interfacial spinodal phase separation for a finite period of time. Significant concentration fluctuations at the GB are observed during the transient spinodal. In this regime, fluctuations in the GB concentration appear and grow and high-concentration regions with ~22 at.% Mn concentration form, while the GB is continuously enriched. The APT analysis confirms these modeling predictions: The Fe9Mn alloy annealed for 6 h at 450 °C shows a similar level of GB segregation with spatial fluctuation corresponding to a transient spinodal phase separation. Once the GB is saturated and the interfacial concentration becomes uniform, the segregation proceeds homogeneously until the equilibrium GB concentration is reached.

The simulated time-dependent concentration line-plots, Fig. 6, compares the normal GB segregation, spinodal phase separation and transient spinodal phase separation within the GB plane (see also Fig. 4). For an alloy with 2.9 at.% Mn, a uniform GB concentration profile develops over time while a GB spinodal decomposition is clearly observed for Fe–3.3 at.% Mn. A transient spinodal decomposition occurs in the Fe–9 at.% Mn alloy. The current results show that the kinetics of GB segregation can be very complex not only close to the spinodal point but also for compositions above the jump composition. The concept of transient spinodal phase separation provides a consistent explanation of the current experimental observations and gives insights for material design purposes that will be discussed in the next section.

DISCUSSION

Segregation of Mn has been considered as one possible cause for GB embrittlement in Fe–Mn alloys, which reduces the mechanical toughness of these alloys[74,75]. This is attributed to GB decohesion due to the Mn segregation[20]. A recent DFT investigation indicates that a higher Mn concentration due to the segregation decreases the
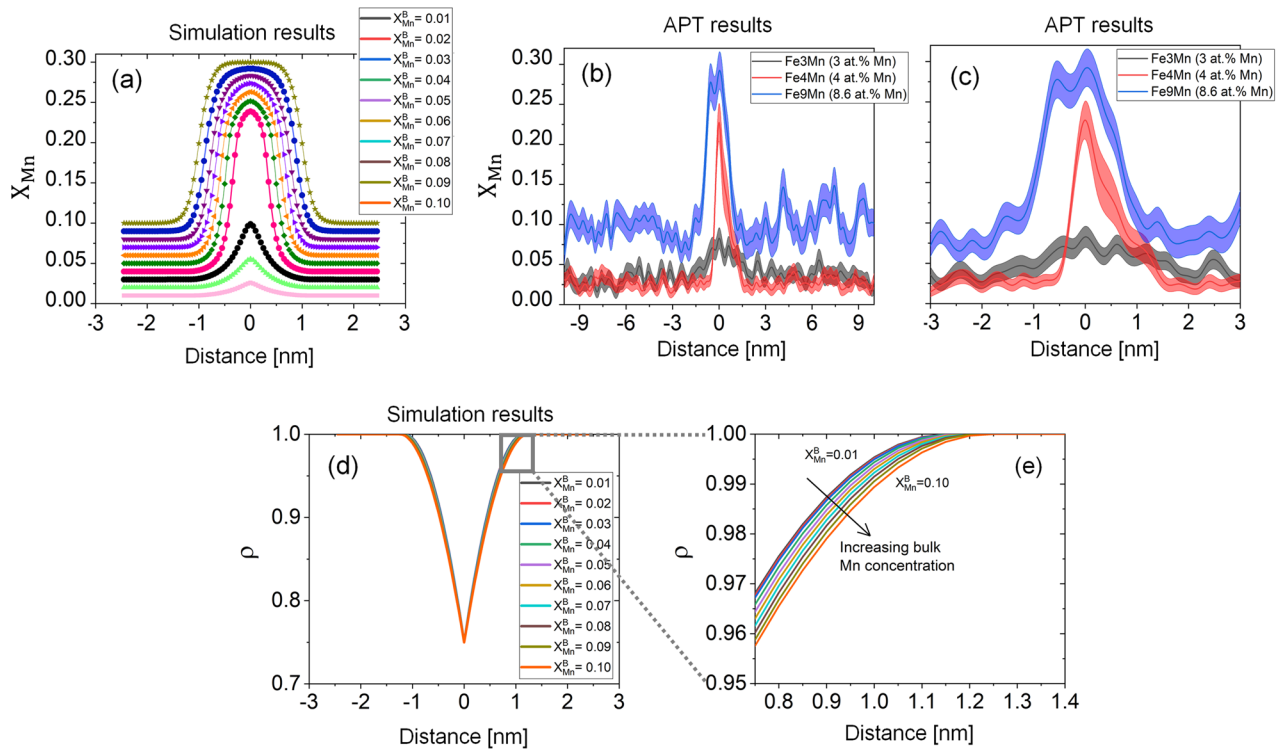
R. Darvishi Kamachali et al.

Fig. 3 Equilibrium GB concentration and density profiles. a Mn concentration profiles are shown for different bulk compositions (1D calculations). An atomic GB density $\rho^{GB} = 0.75$ and a gradient energy coefficient $\kappa_X = 5 \times 10^{-18}$ J m^2 mol^{-1} were used in these calculations. **b, c** Concentration profiles with corresponding error bars obtained from the APT measurements for three different Fe–Mn alloys with 3.0, 4.0, and 8.6 at.% Mn (Fe3Mn, Fe4Mn, and Fe9M, respectively). **b** is magnification of (**c**) along the x axis. A jump in the GB segregation occurs for an alloy composition between 3.0 and 4.0 at.% Mn that is confirmed by APT measurements. **d, e** Equilibrium density profiles for different bulk compositions, corresponding to the concentration profiles in (**a**). For higher segregation levels, the GB width increases.
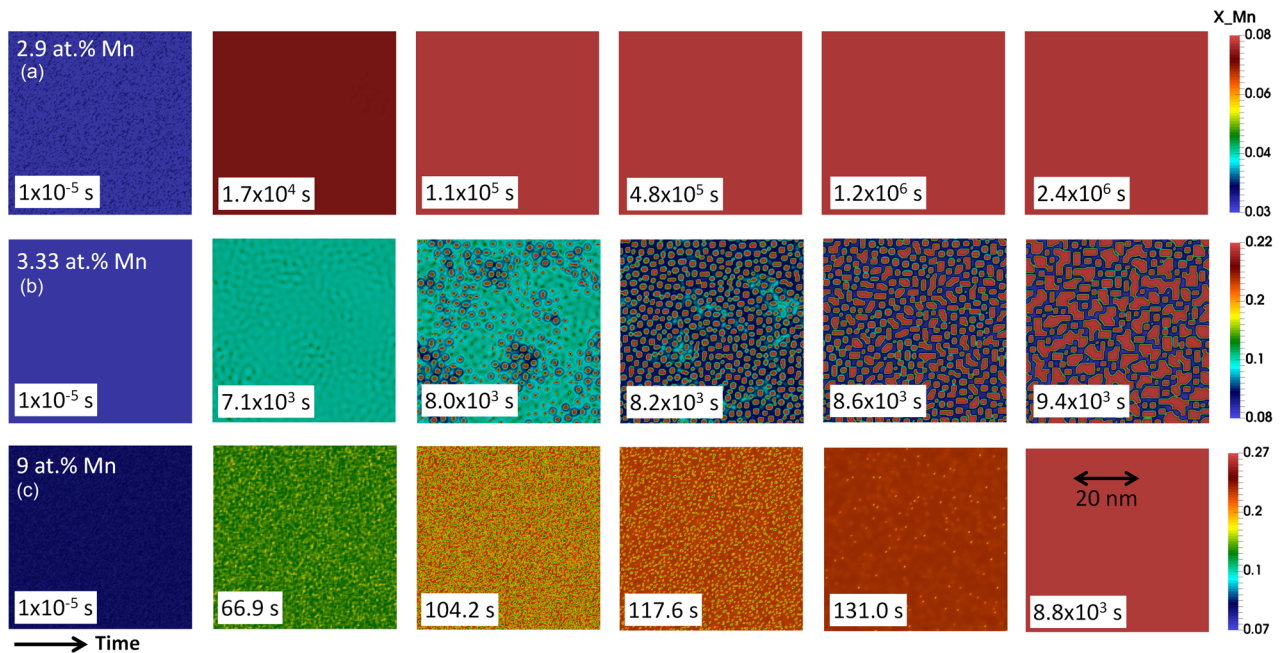

Fig. 4 Time evolution of Mn concentration in the GB plane. 2D cross sections (GB in-plane view) from 3D simulations are shown for three different alloys with **a** 2.9, **b** 3.3, and **c** 9 at.% Mn (450 °C). For an alloy with 3.3 at.% Mn (close to jump composition) an interfacial spinodal phase separation is observed. Above this composition, we have found a transient spinodal regime demonstrated for Fe–9 at.% Mn alloy.

cleavage-fracture energy of the GBs[76]. However, if the Mn segregation level is high enough, it can initiate formation of austenite at the GBs which can partly recover the alloy toughness. Using transmission electron microscopy and near-atomic scale tomographic

measurements, it was shown that reversed austenite layers can form on the Mn-enriched martensite boundaries in a Fe–9 wt% Mn alloy annealed at 450 °C[30,31]. The observed high levels of Mn segregation to the GBs is attributed to a jump in segregation isotherm[37,38].
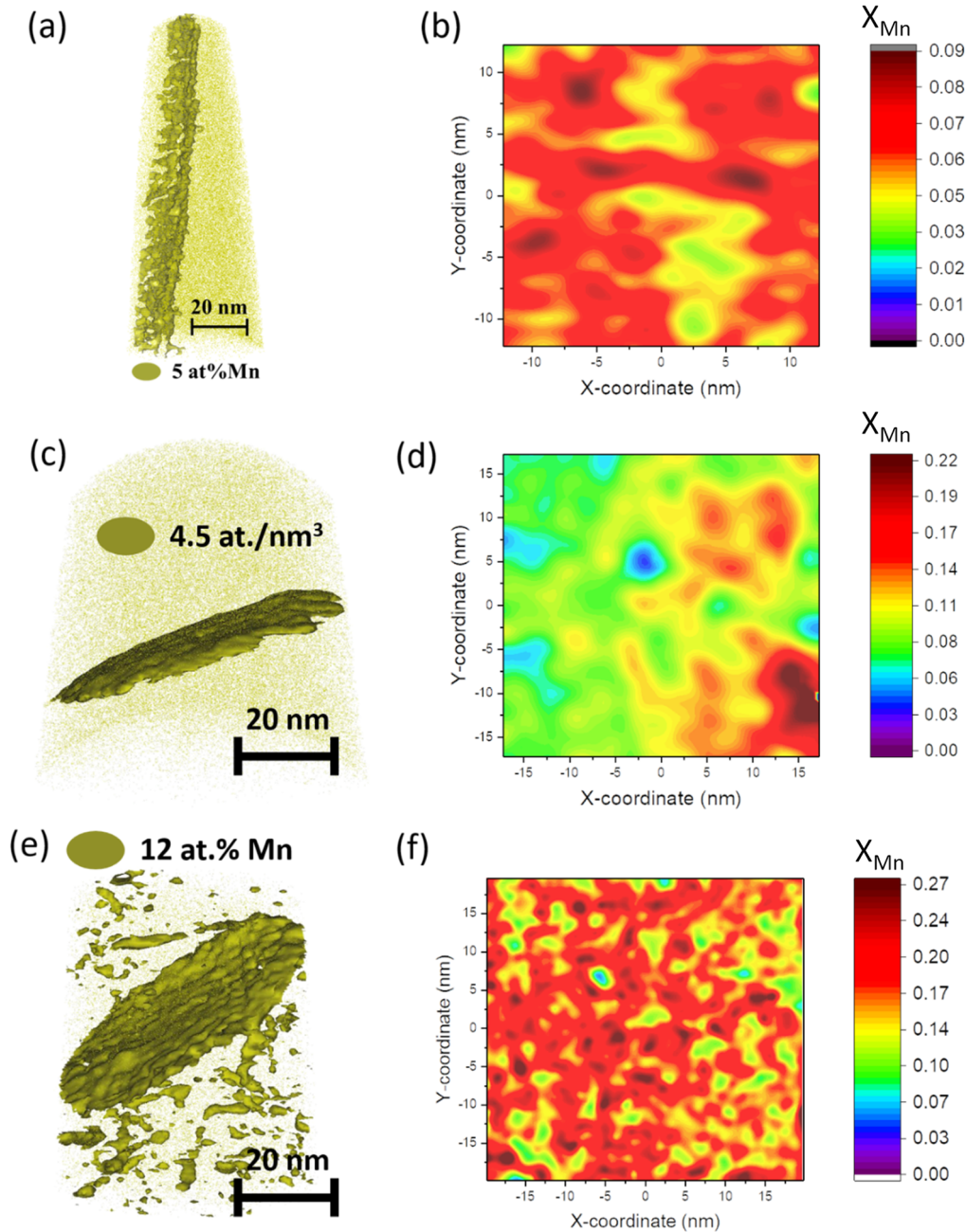
Fig. 5 APT analysis of the Mn concentration. Three alloys with 3.0 at.% Mn (**a, b**), 4.0 at.% Mn (**c, d**), and 8.6 at.% Mn (**e, f**) were studied. The 2D GB in-plane concentration maps are extracted from the 3D APT data, to be comared with simulation results in Fig. 4. The Fe3Mn and Fe4Mn alloys were annealed for 2 months at 450 °C. The Fe9Mn was annealed for 6 h at the same temperature.

In the current study we have quantified the level of Mn segregation in the binary Fe–Mn alloys. Figure 7 shows the GB segregation isotherm for the Fe–Mn system at 450 °C obtained from the current density-based model. The jump in the segregation isotherm corresponds to an interfacial spinodal transition that confirms the abrupt increase in the GB segregation level observed in the experiments. This means that for the jump bulk composition (~3.3 at.% Mn) at 450 °C a two-phase GB is expected to be in equilibrium with a single-phase bulk. Since, however, there is always a small deviation from this critical composition, a stable two-phase GB in equilibrium with the single-phase bulk is difficult to be realized experimentally.

The equilibrium concentration profiles across the GB are shown in Fig. 3 for different alloy compositions. The spread of the Mn segregation in the GB region is determined by the initial bulk composition as well as the concentration gradient coefficient κ_X. The effect of such interfacial concentration gradients is neglected is most of previous works. We show that a larger gradient coefficient results in a wider and smoother segregation profile across the GB and reduces the maximum equilibrium segregation, i.e., it shifts the segregation isotherm towards lower values of GB segregation (Fig. 2). In systems with strong atomic interactions the concentration gradient coefficient can also be composition-dependent[77] rendering the spread of the segregation region composition-dependent as well.

The interfacial spinodal point in the equilibrium segregation isotherm (Fig. 7) separates the low and high GB segregation regimes as a function of alloy composition. The results from our model show that the kinetics of segregation is very different for
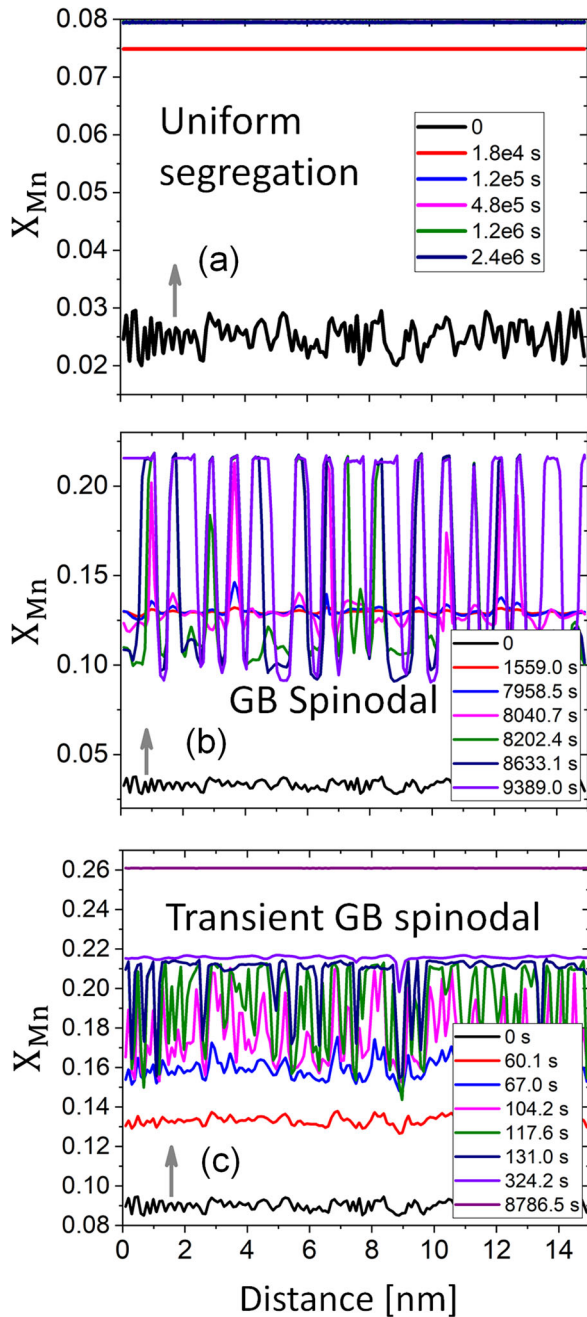
Fig. 6 Simulated time evolution of the Mn concentration in the GB plane. a 2.9, b 3.3, and c 9 at.% Mn alloy compositions were studied. For an 2.9 at.% Mn alloy (below the jump composition), segregation increases monotonically and it is stable even after long simulation times. For a composition very close to the jump composition (3.3 at.% Mn), a spinodal GB phase separation is observed. Above the jump composition (9 at.% Mn) a transient spinodal regime is observed before reaching the equilibrium Mn segregation level.

the low and high segregation levels. In particular, the results of 3D simulations reveal that at 450 °C and for alloy compositions $X^B >$ 0.033, the GBs go through a transient spinodal before reaching a higher uniform Mn segregation level. Figures 4 and 6 show time evolution of the GB concentration for three Fe–Mn alloys. The transient GB spinodal is dictated by the fact that for reaching equal chemical potential (between the bulk and the GB) the segregation must proceed by passing through the GB spinodal
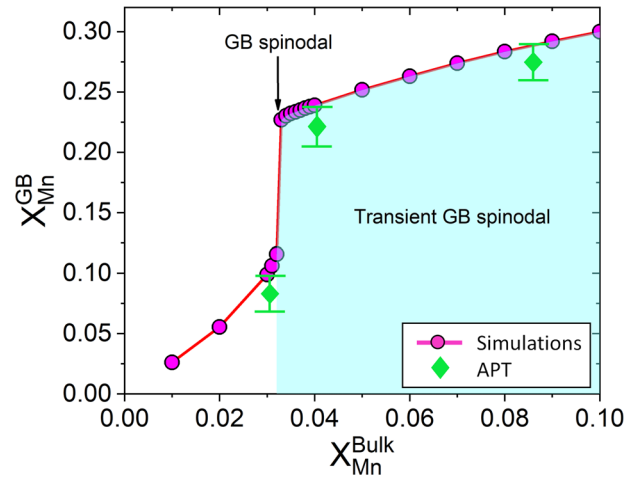

Fig. 7 GB segregation isotherms for the Fe–Mn system at 450 °C. An atomic GB density $\rho^{GB} = 0.75$ and a gradient energy coefficient $\kappa_X = 5 \times 10^{-18}$ J m^2 mol^{-1} were used for these calculations. The abrupt jump in the GB concentration (GB spinodal) is found for an alloy with ~3.33 at.% Mn. Above this composition a transient GB spinodal was revealed through 3D simulations. The green points indicate the highest GB concentration obtained from the APT measurements for alloys with 3.0, 4.0, and 8.6 at.% Mn.

area in the composition space. The chemical potential of the Mn solute atoms (relative to the Fe atoms) reads:

$$\delta\mu(T, \rho, X_{Mn}) = G^0_{Mn} - G^0_{Fe} + \rho^2 \frac{\partial \Delta H^B_{ex}}{\partial X_{Mn}} - T \frac{\partial \Delta S^B_{mix}}{\partial X_{Mn}} - \kappa_X \nabla^2 X_B.$$

(11)

For the sake of discussion, we neglect the last term in this relation and plot the chemical potential as a function of composition. Figure 8a shows the chemical potential of Mn within the bulk ($\rho = 1$) and a GB with an atomic density $\rho = \rho^{GB} = 0.75$ in the absence of gradient energy term. The Maxwell construction is applied here to obtain the equilibrium chemical potentials over the two-phase bulk and GB regions. This construction is equivalent to the common tangent line on the Gibbs free energy curve with the conditions of equal chemical potentials and equal grand potentials[78], i.e., $\delta\mu^p = \delta\mu^q$ and $G^p - \delta\mu^p X^p_{Mn} = G^q - \delta\mu^q X^q_{Mn}$, respectively, in which p and q indicate the two phases in equilibrium. For example, for the bulk FeMn at 450 °C (the black line in Fig. 8a) this gives the equilibrium compositions 0.11 and 0.32, between which the single-phase bulk decomposes to the two phases with 11 and 32 at.% Mn. Similar construction is done for the GB (Fig. 8a, red curve).

As the Mn content in the bulk alloy increases, it is found that above the GB spinodal point and before reaching the bulk spinodal, there is a range of chemical potentials (bulk compositions) that produces the transient GB spinodal phase separation. These are marked with the two-sided black arrows in Fig. 8a. The difference between the bulk and GB chemical potentials arises here due to the enthalpy of mixing (third term in Fig. 11) which quadratically scales with the local density ρ. The magnetic energy plays an important role in the Fe–Mn system[79,80] resulting in an asymmetric enthalpy of mixing over the composition space (see the "Methods" section). This is then responsible for the asymmetric chemical potential over the miscibility gap, observed in Fig. 8a and b. It should be noted that the gradient energy contribution (last term in Eq. (11)) can also have a significant effect on the equilibrium segregation profile as investigated in Fig. 2.

Obviously, different types of GBs with different structures and misorientations may show different density profiles, GB free energy and chemical potential. The average GB density ρ^{GB} can be calculated over the unit area for any given GB. Figure 8b compares the chemical
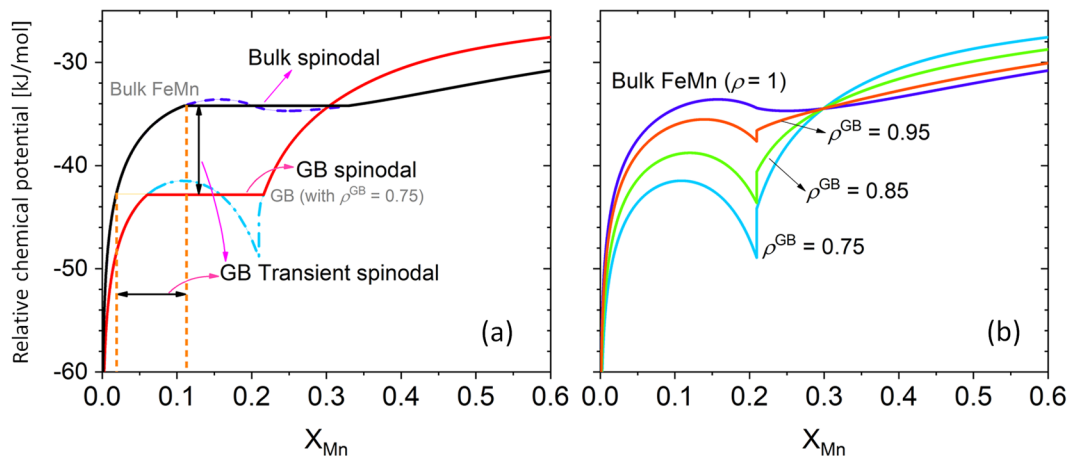
Fig. 8 Mn chemical potential for bulk and different GBs. a The equilibrium chemical potential curves for the bulk and a GB with average atomic density $\rho^{GB} = 0.75$ at 450 °C are compared. The Maxwell construction is applied and the unstable sections of chemical potential curves are shown as dashed lines. Above the GB spinodal, segregation is accompanied with a transient spinodal phenomenon as discussed for the Fe–9 at.% Mn alloy. The range of bulk compositions/chemical potentials for transient GB spinodal are marked with the two-sided black arrows. **b** The chemical potential curves for different GB density values (representing different GB types) are compared. Depending on the GB atomic density, the GB free energy density, the chemical potential and hence the coexistence of the bulk and GB can change.

potential of Mn for three different average GB atomic densities. At a given temperature, a higher GB atomic density value ($\rho^{GB} \rightarrow 1$) represents a GB that behaves more like the corresponding bulk. Hence, the composition/chemical potential window for a transient GB spinodal becomes smaller, as shown in Fig. 8b. Special GBs, e.g., coherent twin boundaries and highly symmetric coincidence site lattice boundaries, with higher average density values closer to the bulk density ($\rho^B = 1$) are expected to show less segregation.

The characteristic GB density ρ^{GB} can be associated with the average 'GB free volume'. Low-angle GBs are expected to show an average atomic density inversely proportional to their misorientation angle. In fact, it has been shown that the average free volume of the low-angle GBs increases as their misorientation angle increases[81]. A larger free volume is equivalent with a smaller GB density. High-angle GBs (with the exception of spacial GBs) have the lowest average atomic density (highest free volume). Hence a transient GB spinodal becomes more probable for high-angle GBs because the difference between the GB spinodal and the bulk spinodal chemical potentials increases, as depicted in Fig. 8. In addition, the elastic interaction between the solute atoms and GB can enhance or suppress the level of segregation and thus the transient spinodal phase separation phenomena. This stems from both homogeneous elastic energy due to the mixing and heterogeneous elastic energy due to the concentration modulations. Wynblatt and coworkers[47,48,82] and Heo et al.[54] studied the effect of elastic interactions on the segregation. The elastic energy effects can be also introduced into the current density-based formulation by considering the elastic energy contribution due to the density variations at the GB and the Vegard's law to describe concentration-dependent strains[83] that is left for a future study.

Considering available bulk thermodynamic data, the current density-based model can provide quantitative understanding of GB segregation and phase separation for different types of GBs. An application of this model has described the effect of GB energy on the GB segregation in a FeMnNiCrCo high-entropy alloy[84]. Using the density-based model, we can also develop GB phase diagrams for studying GB phase stability. This has been recently demonstrated for the binary Pt–Au[65].

The transient GB spinodal, as revealed in the current study, opens a quantitative route to design and tune desired precursor states for subsequent heterogeneous nucleation and phase transformation paths at GBs. In the Fe–Mn system, for instance, formation of reverse austenite at the Mn-enriched GBs plays a critical role in controlling

GB embrittlement[30,31,85,86]. This concept can be further applied for studying formation and growth of GB precipitates and the corresponding precipitate-free zones in precipitation-hardened Al-alloys[87]. Using the transient spinodal concept, several parameters of mechanical processing and heat treatment conditions can be adjusted to obtain desirable microstructures in alloys which are characterized by spatially confined spinodal and phase formation states. While the initial alloy composition defines the thermodynamic feasibility and accessibility of a spinodal phase separation, the adequate thermo-mechanical processing can be applied to alter the GBs types and volume fraction in the system. In addition, the heat treatment conditions control the duration and extent of the transient spinodal phase separation within the system, which strongly relates to thermally-activated solute diffusion properties of the bulk and GBs. A systematic study of these controlling parameters therefore will enable the exploration of the design space for segregation-assisted confined phase changes at lattice defects.

In summary, we have applied a density-based model for studying segregation and confined phase separation at GBs. The current model describes GB thermodynamic properties based on available bulk thermodynamic data. The model was quantitatively benchmarked on binary Fe–Mn system. The atomic density profile across the GB is obtained by atomistic simulations. Depending on the bulk composition, low and high levels of equilibrium Mn segregations were observed in the Fe–Mn system which are separated by a jump in segregation isotherm (Fig. 7). This jump corresponds to a segregation-assisted spinodal phase separation at the GB. Our studies reveal a transient GB spinodal phase separation for alloy compositions beyond the jump. Considering the transient spinodal phenomenon, the GB segregation and phase separation in the Fe–Mn alloys were consistently explained. The current density-based model and the demonstrated quantitative understanding about the segregation and the transient spinodal phase separation at GBs provides a powerful means for achieving desirable microstructures by the knowledge-based variation of alloying and processing parameters.

METHODS

Density-based phase-field calculations

We simulate a single flat GB section separating two large grains. This is a subset of a large-grain Fe–Mn polycrystalline alloy sample with free surfaces, as in our experiments, heat treated at constant temperature and pressure. The large-grain assumption implies that (i) the total amount of segregation is
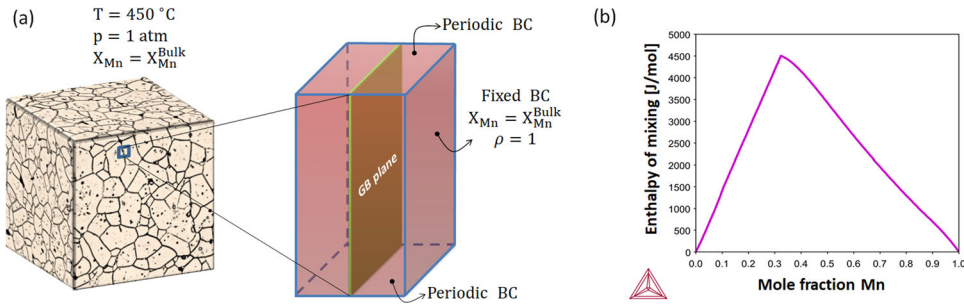
Fig. 9 Simulation set-up. a The large-grain polycrystalline sample and the simulation set-up of a single flat GB are schematically shown. We apply fixed boundary conditions parallel to the GB plane while other boundaries are periodic. **b** The enthalpy of mixing of Fe–Mn system is shown at 450 °C.

Table 1. Input parameters for the current simulation studies.

Parameter	Values	Physical dimension	Source
E_A^B (for BCC Fe)	−4479.4	J mol^{-1}	ThermoCalc database
S_A^B (for BCC Fe)	53.1	J K^{-1} mol^{-1}	ThermoCalc database
ρ^{GB}	0.65–0.85	–	Atomistic simulations
η_A	$0.6-1.5 \times 10^{-9}$	m	Atomistic simulations
κ_ρ	$1.63-10.2 \times 10^{-16}$	J m^2 mol^{-1}	Model (Eq. (9))
γ_A	1.28	J m^{-2}	Atomistic simulations
κ_X	$0.05-1 \times 10^{-16}$	J m^2 mol^{-1}	Model (Eq. (10))
M	$1.34 \times 10^{-26} e^{19.0 X_{Mn}}$	mol m^2 J^{-1} s^{-1}	ThermoCalc
L	1×10^{-7}	mol J^{-1} s^{-1}	–
$V_m^{BCC\,Fe}$	7.2×10^{-6}	m^3 mol^{-1}	ThermoCalc

much smaller than the total number of solute atoms in the polycrystalline and (ii) GBs are separated far enough to not affect each other. The free surface condition implies that the polycrystalline sample can freely expand/contract to maintain constant pressure. The simulation domain considered here is therefore open with respect to both the total number of atoms and the total number of solute atoms. These are applied by the fixed boundary conditions $\rho = 1$ and $X_{Mn} = X_{Mn}^{Bulk}$ parallel to the GB plane, while other boundaries of the simulation domain are periodic. Figure 9a shows the simulation set-up schematically. All calculations were done for $T = 450\,°C$ and $p = 1$ atm. For such open system at constant T and p, the Gibbs free energy is the appropriate thermodynamic potential[67–69]. A narrated video presentation of the model's implementation can be found in the Supplementary Video 1.

In order to perform the density-based phase-field simulations, an OpenMP parallel C++ code was developed to solve Equations (6) and (7) numerically. A finite difference scheme with adaptive time stepping has been used. We use $dx = 0.1$ nm and initial $dt = 10^{-5}$ s. In all simulations, uniform Mn concentrations were initialized with random fluctuations of ≤±1 at.%. The thermodynamic data for the BCC Fe–Mn system (up to 30 at. % Mn) were obtained from ThermoCalc TCFE9 and MOB04 databases. The assymetric enthalpy of mixing for Fe–Mn system is shown in Fig. 9b. The GB properties are obtained using atomistic simulations. We apply a coarse-graining scheme to obtain continuous atomic density filed across the GB, as discussed in the next section. Physical parameters are presented in Table 1. All quantities are scaled by the BCC Fe molar volume to obtain respective values per unit volume. For the Mn atoms, the composition-dependent mobility from ThermoCalc database was fitted as

$$M = 1.3993 \times 10^{-26} \exp(19.0375 \, X_{Mn}) \tag{12}$$

in unit m^2 mol^{-1} s^{-1} that indicates a rapid increase in the atomic mobility as a function of Mn concentration. For more information about the thermodynamic and kinetic databases, see refs. [88–93]. The simulation results are extracted and visualized using Paraview[94].

Atomistic calculations

In order to obtain realistic values for the GB atomic density ρ^{GB}, explicit atomistic simulations have been performed within the environmental
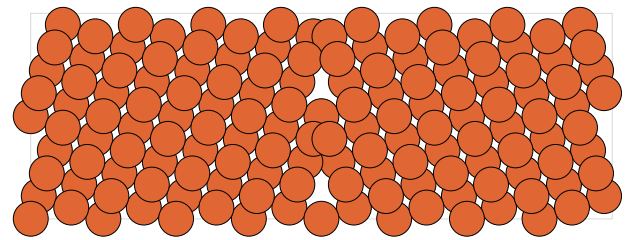

Fig. 10 Atomistic GB structure. The structure of the $\Sigma 9\{122\}[1\bar{1}0]$ symmetric tilt GB in α-Fe.

tight-binding approach[70,71]. This approach enables a fully quantum-mechanical parameter-free description of the energetics and forces of systems of arbitrary chemical complexity, while remaining sufficiently efficient so as to examine a broad variety of microstructural defects. In the present case, we consider a symmetric tilt GB, namely the $\Sigma 9\{122\}[1\bar{1}0]$, in α-Fe. A 144-atom supercell for this GB has been generated, and the structural parameters and internal coordinates have been fully relaxed within the tight-binding method. The resulting atomistic structure is illustrated in Fig. 10.

From the atomistic simulation, we calculate the GB energy density γ_A. However, in order to obtain the atomic density field ρ^{GB}, we have to establish a connection between the discrete atomic structure of the GB and the continuous atomic density function as introduced in the current density-based phase-field model. In the present case, this is done by a coarse-graining step. We replace the atomistically-obtained density function

$$\rho(r) = \sum_I \delta(r - R_I) \tag{13}$$

with R_I being the set of positions of the atoms, with a smeared-out density function, where the delta functions of Eq. (13) are replaced by a normalized

Table 2. The composition of the alloys studied in this work.

Alloy	Mn	C	Ni	Al	S	P	O	N	Fe
Fe9Mn	8.46 (8.60 at.%)	0.0075	0.0175	<0.002	0.0047	<0.002	0.0102	0.0040	Balance
Fe4Mn	3.92 (4.0 at.%)	0.0081	0.0172	<0.002	0.0036	<0.002	0.0096	0.0071	Balance
Fe3Mn	2.95 (3.0 at.%)	0.0079	0.0214	<0.001	0.0028	<0.002	0.0196	0.0024	Balance

Gaussian

$$\delta(x) = \frac{e^{-\frac{x^2}{2\beta^2}}}{\sqrt{2\pi}\,\beta} \tag{14}$$

with a prescribed coarse-graining length β, so that the continuous atomic density profile becomes a smooth function in real space. The parameter β should be at least of the order of the interatomic spacing ($a \sim 2.5$ Å) in the material. As discussed in ref. [65], a physically-motivated coarse-graining radius is the cut-off radius (~4 Å) over which the atomistic forces are calculated. A higher value of β results in a smoother atomic density profile, but with the possible cost of being unable to resolve certain features of the GB itself. We examine three choices of the parameter β close to the cut-off radius as discussed in Fig. 1.

Experiments and APT analysis

Three binary Fe–Mn alloys, identified with 3.0, 4.0, 8.6 at.% Mn, referred to as Fe3Mn, Fe4Mn, and Fe9Mn, were cast into a rectangular billet in a vacuum induction furnace. The composition of the alloys is shown in Table 2 according to wet chemical analysis. The slabs were hot-rolled at 1100 °C from 60- to 6-mm thickness and then water quenched. Subsequently, highly segregated edges of the slab were cut off. The billets were reheated to 1100 °C for 1 h and water quenched to room temperature to minimize Mn banding. After water quenching from the homogenizing temperature, the alloys were fully ferritic without retained austenite. The mechanisms of transformation from austenite to ferrite were martensitic transformation for the Fe9Mn alloy and massive transformation for the Fe3Mn and Fe4Mn alloys. The Fe9Mn was annealed for 6 h, while the two other alloys were subsequently annealed up to 2 months at 450 °C in order to characterize the equilibrium amount of segregation at the GBs. The Fe9Mn and Fe4Mn alloys are situated in the two-phase region of the phase diagram (ferrite and austenite are stable phases). The Fe3Mn alloy is situated in the single-phase field of the phase diagram (ferrite is the only stable phase).

APT specimens with end radii below 100 nm were prepared using a FEI Helios NanoLab600i dual-beam focused ion beam (FIB)/scanning electron microscopy (SEM) instrument. APT was performed using a LEAP 5000 XS device by Cameca Scientific Instruments, with ~80% detection efficiency, at a set-point temperature of 50 K in laser-pulsing mode at a wavelength of 355 nm, 500 kHz pulse repetition rate, and 30 pJ pulse energy. For reconstructing 3D atom maps, visualization and quantification of segregation the commercial software IVAS by Cameca was employed following the protocol introduced by Geiser et al.[95] and detailed in Gault et al.[96]. The 3D-mapping was obtained by the voltage-based reconstruction of the detected ions. The reconstructions were calibrated by the interplanar distance of the crystallographic planes associated with the low-hit density poles.

DATA AVAILABILITY

The numerical and experimental data from this study are available upon reasonable request.

CODE AVAILABILITY

The density-based phase-field code from this study is available upon reasonable request.

REFERENCES

1. Sutton, A. & Balluffi, R. *Interfaces in Crystalline Materials*. (Clarendon Press, Oxford, 1995).
2. Gottstein, G. & Shvindlerman, L. S. *Grain Boundary Migration in Metals: Thermodynamics, Kinetics, Applications* (CRC Press, 2009).
3. Watanabe, T. & Tsurekawa, S. The control of brittleness and development of desirable mechanical properties in polycrystalline systems by grain boundary engineering. *Acta Mater.* **47**, 4171–4185 (1999).
4. Lejček, P., Hofmann, S. & Paidar, V. Solute segregation and classification of [100] tilt grain boundaries in α-iron: consequences for grain boundary engineering. *Acta Mater.* **51**, 3951–3963 (2003).
5. Randle, V. Twinning-related grain boundary engineering. *Acta Mater.* **52**, 4067–4081 (2004).
6. Watanabe, T. Grain boundary engineering: historical perspective and future prospects. *J. Mater. Sci.* **46**, 4095–4115 (2011).
7. Raabe, D. et al. Grain boundary segregation engineering in metallic alloys: a pathway to the design of interfaces. *Curr. Opin. Sol. Stat. Mater. Sci.* **18**, 253–261 (2014).
8. Gibbs, J. W. *The Collected Works of J. Willard Gibbs* Vol 1–2. (Yale University Press, London, 1957).
9. Straumal, B. et al. Premelting transition on 38°⟨100⟩ tilt grain boundaries in (Fe-10 at.% Si)-Zn alloys. *Acta Metal. Mater.* **40**, 795–801 (1992).
10. Dillon, S. J. & Harmer, M. P. Multiple grain boundary transitions in ceramics: a case study of alumina. *Acta Mater.* **55**, 5247–5254 (2007).
11. Dillon, S. J., Tang, M., Carter, W. C. & Harmer, M. P. Complexion: a new concept for kinetic engineering in materials science. *Acta Mater.* **55**, 6208–6218 (2007).
12. Kundu, A., Asl, K. M., Luo, J. & Harmer, M. P. Identification of a bilayer grain boundary complexion in bi-doped cu. *Scr. Mater.* **68**, 146–149 (2013).
13. Cantwell, P. R. et al. Grain boundary complexions. *Acta Mater.* **62**, 1–48 (2014).
14. Jorgensen, P. & Anderson, R. Grain-boundary segregation and final-stage sintering of Y₂O₃. *J. Am. Ceram. Soc.* **50**, 553–558 (1967).
15. Gupta, D. Influence of solute segregation on grain-boundary energy and self-diffusion. *Metal. Trans. A* **8**, 1431–1438 (1977).
16. Bernardini, J., Gas, P., Hondros, E. D. & Seah, M. The role of solute segregation in grain boundary diffusion. *Proc. Roy. Soc. Lon. A. Math. Phys. Sci.* **379**, 159–178 (1982).
17. Kirchheim, R. Grain coarsening inhibited by solute segregation. *Acta Mater.* **50**, 413–419 (2002).
18. Mendelev, M., Srolovitz, D., Ackland, G. & Han, S. Effect of fe segregation on the migration of a non-symmetric Σ5 tilt grain boundary in al. *J. Mater. Res.* **20**, 208–218 (2005).
19. Darvishi Kamachali, R. *Grain Boundary Motion in Polycrystalline Materials*. Ph.D. thesis, Univ.-Bibliothek (2013).
20. Seah, M. Adsorption-induced interface decohesion. *Acta Metal.* **28**, 955–962 (1980).
21. Kumar, A. & Eyre, B. L. Grain boundary segregation and intergranular fracture in molybdenum. *Proc. Roy. Soc. Lon. A. Math. Phys. Sci.* **370**, 431–458 (1980).
22. White, C., Liu, C., Padgett, R. & Yalisove, S. Surface and grain boundary segregation in relation to intergranular fracture: boron and sulfur in Ni₃Al. *Scr. Metal.* **18**, 1417–1420 (1984).
23. Song, R. et al. Grain boundary segregation and hydrogen-induced fracture in 7050 aluminium alloy. *Acta Mater.* **44**, 3241–3248 (1996).
24. De Hass, M. & De Hosson, J. T. M. Grain boundary segregation and precipitation in aluminium alloys. *Scr. Mater.* **44**, 281–286 (2001).
25. Hin, C., Bréchet, Y., Maugis, P. & Soisson, F. Kinetics of heterogeneous grain boundary precipitation of nbc in α-iron: a monte carlo study. *Acta Mater.* **56**, 5653–5667 (2008).
26. Darvishi Kamachali, R. & Schwarze, C. Inverse ripening and rearrangement of precipitates under chemomechanical coupling. *Comp. Mater. Sci.* **130**, 292–296 (2017).
27. Li, B. et al. Simulations of irradiated-enhanced segregation and phase separation in Fe–Cu–Mn alloys. *Model. Sim. Mater. Sci. Eng.* **25**, 065007 (2017).

28. Park, J. et al. First evidence for mechanism of inverse ripening from in-situ TEM and phase-field study of δ' precipitation in an Al-Li alloy. *Sci. Rep.* **9**, 3981 (2019).

29. Enomoto, M., Nojiri, N. & Sato, Y. Effects of vanadium and niobium on the nucleation kinetics of proeutectoid ferrite at austenite grain boundaries in FeC and Fe-CMn alloys. *Mater. Trans.* **35**, 859–867 (1994).

30. Raabe, D. et al. Segregation engineering enables nanoscale martensite to austenite phase transformation at grain boundaries: a pathway to ductile martensite. *Acta Mater.* **61**, 6132–6152 (2013).

31. Kuzmina, M., Ponge, D. & Raabe, D. Grain boundary segregation engineering and austenite reversion turn embrittlement into toughness: example of a 9 wt.% medium Mn steel. *Acta Mater.* **86**, 182–192 (2015).

32. Rabkin, E., Shvindlerman, L. S. & Straumal, B. B. Grain boundaries: phase transitions and critical phenomena. *Inter. J. Mod. Phys. B* **5**, 2989–3028 (1991).

33. Luo, J., Gupta, V., Yoon, D. & Meyer III, H. Segregation-induced grain boundary premelting in nickel-doped tungsten. *Appl. Phys. Lett.* **87**, 231902 (2005).

34. Fowler, R. & Guggenheim, E. A. *Statistical Thermodynamics* (Cambridge U. Press, 1965).

35. Hart, E. W. Two-dimensional phase transformation in grain boundaries. *Scr. Metal.* **2**, 179–182 (1968).

36. Hu, A. *The Nature and Behavior of Grain Boundaries: A Symposium Held at the TMS-AIME Fall Meeting in Detroit, Michigan, October 18–19, 1971* (Springer Science & Business Media, 2012).

37. Kwiatkowski Da Silva, A. et al. Phase nucleation through confined spinodal fluctuations at crystal defects evidenced in Fe-Mn alloys. *Nat. Comm.* **9**, 1137 (2018).

38. Kwiatkowski da Silva, A. et al. Thermodynamics of grain boundary segregation, interfacial spinodal and their relevance for nucleation during solid-solid phase transitions. *Acta Mater.* **168**, 109–120 (2019).

39. Langmuir, I. The adsorption of gases on plane surfaces of glass, mica and platinum. *J. Am. Chem. Soc.* **40**, 1361–1403 (1918).

40. McLean, D. *Grain Boundaries in Metals* (1957).

41. Hondros, E. & Seah, M. The theory of grain boundary segregation in terms of surface adsorption analogues. *Metal. Trans. A* **8**, 1363–1371 (1977).

42. Seah, M. Grain boundary segregation. *J. Phys. F: Met. Phys.* **10**, 1043 (1980).

43. Lejček, P. & Hofmann, S. Thermodynamics and structural aspects of grain boundary segregation. *Crit. Rev. Sol. Stat. Mater. Sci.* **20**, 1–85 (1995).

44. Kirchheim, R. Reducing grain boundary, dislocation line and vacancy formation energies by solute segregation. i. theoretical background. *Acta Mater.* **55**, 5129–5138 (2007).

45. Lejček, P. & Hofmann, S. Modeling grain boundary segregation by prediction of all necessary parameters. *Acta Mater.* **170**, 253–267 (2019).

46. Lejček, P. in *Grain Boundary Segregation in Metals*, 5–24 (Springer, 2010).

47. Wynblatt, P. & Shi, Z. Relation between grain boundary segregation and grain boundary character in fcc alloys. *J. Mater. Sci.* **40**, 2765–2773 (2005).

48. Wynblatt, P. & Chatain, D. Anisotropy of segregation at grain boundaries and surfaces. *Metal. Mater. Trans. A* **37**, 2595–2620 (2006).

49. Cahn, J. W. Critical point wetting. *J. Chem. Phys.* **66**, 3667–3672 (1977).

50. Cha, P.-R., Kim, S. G., Yeon, D.-H. & Yoon, J.-K. A phase field model for the solute drag on moving grain boundaries. *Acta Mater.* **50**, 3817–3829 (2002).

51. Hu, S., Choi, J., Li, Y. & Chen, L. Dynamic drag of solute atmosphere on moving edge dislocationsphase-field simulation. *J. Appl. Phys.* **96**, 229–236 (2004).

52. Grönhagen, K. & Ågren, J. Grain-boundary segregation and dynamic solute drag theory—a phase-field approach. *Acta Mater.* **55**, 955–960 (2007).

53. Kim, S. G. & Park, Y. B. Grain boundary segregation, solute drag and abnormal grain growth. *Acta Mater.* **56**, 3739–3753 (2008).

54. Heo, T. W., Bhattacharyya, S. & Chen, L.-Q. A phase field study of strain energy effects on solute–grain boundary interactions. *Acta Mater.* **59**, 7800–7815 (2011).

55. Hu, S. & Chen, L.-Q. Solute segregation and coherent nucleation and growth near a dislocationa phase-field model integrating defect and phase microstructures. *Acta Mater.* **49**, 463–472 (2001).

56. Ma, N., Dregia, S. & Wang, Y. Solute segregation transition and drag force on grain boundaries. *Acta Mater.* **51**, 3687–3700 (2003).

57. Ma, N., Shen, C., Dregia, S. & Wang, Y. Segregation and wetting transition at dislocations. *Metal. Mater. Trans. A* **37**, 1773–1783 (2006).

58. Mishin, Y. Solute drag and dynamic phase transformations in moving grain boundaries. *Acta Mater.* **179**, 383 – 395 (2019).

59. Kobayashi, R., Warren, J. A. & Carter, W. C. A continuum model of grain boundaries. *Phys. D: Nonlin. Phenom.* **140**, 141–150 (2000).

60. Tang, M., Carter, W. C. & Cannon, R. M. Diffuse interface model for structural transitions of grain boundaries. *Phys. Rev. B* **73**, 024102 (2006).

61. Tang, M., Carter, W. C. & Cannon, R. M. Grain boundary order-disorder transitions. *J. Mater. Sci.* **41**, 7691–7695 (2006).

62. Tang, M., Carter, W. C. & Cannon, R. M. Grain boundary transitions in binary alloys. *Phys. Rev. Lett.* **97**, 075502 (2006).

63. Kim, S. G., Lee, J. S. & Lee, B.-J. Thermodynamic properties of phase-field models for grain boundary segregation. *Acta Mater.* **112**, 150–161 (2016).

64. Kim, S. G., Kim, W. T. & Suzuki, T. Phase-field model for binary alloys. *Phys. Rev. E* **60**, 7186 (1999).

65. Darvishi Kamachali, R. A model for grain boundary thermodynamics. *RSC Adv.* **10**, –26741 (2020).

66. van der Waals, J. D. The thermodynamic theory of capillarity under the hypothesis of a continuous variation of density. *J. Stat. Phys.* **20**, 200–244 (1979).

67. Olla, P. *An Introduction to Thermodynamics and Statistical Physics* (Springer, 2015).

68. Tsao, J. Y. *Materials Fundamentals of Molecular Beam Epitaxy* (Academic Press, 2012).

69. Newman, J. *Physics of the Life Sciences* (Springer Science & Business Media, 2010).

70. McEniry, E. J., Drautz, R. & Madsen, G. Environmental tight-biding modeling of nickel and cobalt clusters. *J. Phys.: Condens. Matter* **25**, 115502 (2013).

71. McEniry, E. J., Hickel, T. & Neugebauer, J. Hydrogen behaviour at twist {110} grain boundaries in α-Fe. *Philos. Trans. A* **375**, 20160402 (2017).

72. Haile, J. *Molecular Dynamics Simulation: Elementary Methods* (Weily, 1997).

73. Cahn, J. W. & Hilliard, J. E. Free energy of a nonuniform system. I. Interfacial free energy. *J. Chem. Phys.* **28**, 258–267 (1958).

74. Takayama, S., Ogura, T., Fu, S.-C. & McMahon, C. The calculation of transition temperature changes in steels due to temper embrittlement. *Metal. Trans. A* **11**, 1513 (1980).

75. Han, J. et al. The effects of prior austenite grain boundaries and microstructural morphology on the impact toughness of intercritically annealed medium Mn steel. *Acta Mater.* **122**, 199–206 (2017).

76. Ito, K., Sawada, H. & Ogata, S. First-principles study on the grain boundary embrittlement of bcc-Fe by Mn segregation. *Phys. Rev. Mater.* **3**, 013609 (2019).

77. Lass, E. A., Johnson, W. C. & Shiflet, G. J. Correlation between CALPHAD data and the Cahn–Hilliard gradient energy coefficient κ and exploration into its composition dependence. *Calphad* **30**, 42–52 (2006).

78. Kondepudi, D. & Prigogine, I. *Modern Thermodynamics: from Heat Engines to Dissipative Structures* (John Wiley & Sons, 2014).

79. Hillert, M. & Jarl, M. A model for alloying in ferromagnetic metals. *Calphad* **2**, 227–238 (1978).

80. Witusiewicz, V., Sommer, F. & Mittemeijer, E. Reevaluation of the Fe-Mn phase diagram. *J. Phas. Equil. Diff.* **25**, 346–354 (2004).

81. Aaron, H. & Bolling, G. Free volume as a criterion for grain boundary models. *Surf. Sci.* **31**, 27–49 (1972).

82. Wynblatt, P. & Ku, R. Surface energy and solute strain energy effects in surface segregation. *Surf. Sci.* **65**, 511–531 (1977).

83. Khachaturyan, A. G. *Theory of Structural Transformations in Solids* (Courier Corporation, 2013).

84. Li, L., Darvishi Kamachali, R., Li, Z. & Zhang, Z. Grain boundary energy effect on grain boundary segregation in an equiatomic high-entropy alloy. *Phys. Rev. Mater.* **4**, 053603 (2020).

85. Wang, M.-M., Tasan, C. C., Ponge, D., Dippel, A.-C. & Raabe, D. Nanolaminate transformation-induced plasticity–twinning-induced plasticity steel with dynamic strain partitioning and enhanced damage resistance. *Acta Mater.* **85**, 216–228 (2015).

86. Koyama, M. et al. Bone-like crack resistance in hierarchical metastable nanolaminate steels. *Science* **355**, 1055–1057 (2017).

87. Häusler, I. et al. Precipitation of T_1 and θ' phase in Al-4Cu-1Li-0.25 Mn during age hardening: microstructural investigation and phase-field simulation. *Materials* **10**, 117 (2017).

88. Dinsdale, A. SGTE data for pure elements. *Calphad* **15**, 317–425 (1991).

89. Djurovic, D., Hallstedt, B., Von Appen, J. & Dronskowski, R. Thermodynamic assessment of the Fe–Mn–C system. *Calphad* **35**, 479–491 (2011).

90. Liu, S., Hallstedt, B., Music, D. & Du, Y. Ab initio calculations and thermodynamic modeling for the Fe–Mn–Nb system. *Calphad* **38**, 43–58 (2012).

91. Liu, Y., Zhang, L., Du, Y., Yu, D. & Liang, D. Atomic mobilities, uphill diffusion and proeutectic ferrite growth in Fe–Mn–C alloys. *Calphad* **33**, 614–623 (2009).

92. Messina, L., Nastar, M., Garnier, T., Domain, C. & Olsson, P. Exact ab initio transport coefficients in bcc Fe- X = Cr, Cu, Mn, Ni, P, Si) dilute alloys. *Phys. Rev. B* **90**, 104203 (2014).

93. Deng, S. et al. Diffusion study in bcc–A2 Fe-Mn-Si system: experimental measurement and CALPHAD assessment. *Calphad* **56**, 230–240 (2017).

94. Ayachit, U. *The Paraview Guide: A Parallel Visualization Application* (Kitware, Inc., 2015).

95. Geiser, B. et al. Wide-field-of-view atom probe reconstruction. *Micros. Microanal.* **15**, 292–293 (2009).
96. Gault, B. et al. Advances in the reconstruction of atom probe tomography data. *Ultramicroscopy* **111**, 448–457 (2011).

ACKNOWLEDGEMENTS

AUTHOR CONTRIBUTIONS

R.D.K. devised the density-based model, performed the simulations, and wrote the manuscript; A.K.S. performed the experiments and APT studies; A.K.S., D.R., D.P., and B.G. conceived and supervised the experiments and APT analysis; E.M. conducted the atomistic simulation studies; J.N. supervised and discussed the simulation results; all authors reviewed the manuscript.

FUNDING

COMPETING INTERESTS

The authors declare no competing interests.

ADDITIONAL INFORMATION

Supplementary information is available for this paper at https://doi.org/10.1038/s41524-020-00456-7.

Correspondence and requests for materials should be addressed to R.D.K.

Reprints and permission information is available at http://www.nature.com/reprints

Publisher's note Springer Nature remains neutral with regard to jurisdictional claims in published maps and institutional affiliations.